Second International Symposium on Marine Propulsors
smp'11, Hamburg, Germany, June 2011

Modeling of Leading Edge Vortex and its Effects on Propeller Performance*

Ye Tian[1] and Spyros Kinnas[2]

[1,2] Ocean Engineering Group, Department of Civil and Environmental Engineering, University of Texas at Austin, Austin, TX, USA

ABSTRACT

A numerical model for the leading edge vortex (LEV) sheet is developed, in both 2D and 3D cases. LEV rolling-up is first investigated for 2-D biconvex foil. The LEV geometry and corresponding pressure distribution are compared with the results from inviscid finite volume method and RANS. The 3D extension of the LEV model is applied to delta wings, and also propeller geometries. The results from the LEV model are correlated with results from RANS. In the case of propeller, the results are compared with experimental measurements.

Keywords

Leading edge vortex, boundary element method, propeller performance

1 INTRODUCTION

At high loading, a vortex sheet separates from the leading edge region of a propeller blade. This vortex sheet passes over the propeller blade and significantly changes the load distribution. On moderately high loading conditions, the shed leading edge vortex (LEV) sheet also alters the flow patterns near the tip of the propeller blade. LEV is connected with the trailing edge wake, forming complicated roll-up geometry. The cavities brought in by LEV also make the propeller tip flow more entangled. Because of the special geometry of the tip of a blade, it usually requires very dense and high-quality cells for 3-D RANS simulations. Obviously, the cost of RANS is unacceptable in the design stage. Therefore, an efficient and accurate numerical model for propeller tip flow has been in demand for many years.

An early study on propeller tip flow was conducted by Greeley (1982). He essentially treated the LEV with a combination of empirical and numerical methods. Later, Lee et al (2002, 2004) developed a 3-D wake model based on low order panel method for marine propeller, which is able to predict developed tip vortex cavity. The tip vortex cavity is modeled with a cylindrical vortex tube. L. He (2010) extended Lee's wake model in order to be able to take some viscous effects into account. In He's study, different viscous core was tested. Singh (2009) applied He's algorithm to 2D hydrofoils with LEV separation, and obtained some preliminary results.

In this paper, LEV roll-up is first investigated for 2-D hydrofoils. A 3-D extension of the 2-D vortex blob method is carried out on 3-D delta wings, which are well-known for strong LEV roll-up effects. After validating the 3-D LEV model with delta wings, the model is applied to propeller geometry. Results for the 2D foil and 3D delta wing cases from the LEV model are compared with results from RANS simulations.

2 FORMULATION

The velocity flow field is decomposed into two components: inflow velocity and perturbation velocity, written as:

$$\boldsymbol{q} = \boldsymbol{U}_\infty + \boldsymbol{u}, \tag{1}$$

where $\boldsymbol{q}$ is the total velocity, $\boldsymbol{U}_\infty$ is the inflow velocity, and $\boldsymbol{u}$ is the perturbation velocity due to the presence of obstacles.

2.1 Governing Equations

The methodology applied in this study is based on the inviscid potential flow theory:

$$\boldsymbol{u} = \nabla\phi, \tag{2}$$

where ϕ is the perturbation potential. The perturbation velocity field therefore is governed by the Laplace Equation:

$$\nabla^2\phi = 0 \tag{3}$$

If the inflow is also irrotational, we can also define the total potential Φ as:

$$\boldsymbol{q} = \nabla\phi + U_\infty = \nabla\Phi, \tag{4}$$

Appling Green's second identity, the Laplace equation (3) can be written as following boundary integrated form:

$$\begin{aligned} 2\pi\phi_p &= \iint_{S_H} \left[\phi_p \frac{\partial G(p,q)}{\partial \boldsymbol{n}_q} - \frac{\partial \phi_p}{\partial \boldsymbol{n}_q} G(p,q)\right] dS \\ &+ \iint_{S_W} \Delta\phi_w(y_q) \frac{\partial G(p,q)}{\partial \boldsymbol{n}_q} dS \\ &+ \iint_{S_{LEV}} \Delta\phi_{LEV}(y_q) \frac{\partial G(p,q)}{\partial \boldsymbol{n}_q} dS, \end{aligned} \tag{5}$$

where S_H represents the surface of hydrofoil or propeller blades; S_W represents the surface of trailing edge wake, and S_{LEV} represents the surface of leading edge vortex. $G(p,q)$ is the Green's function, which is defined as $1/R(p;q)$ in 3D, and $2\ln R(p;q)$ in 2D. A low order panel method using constant dipole panels is adopted to solve Eqn. (5).

2.2 Boundary Conditions

2.2.1 Kinematic boundary condition

Applying the kinematic boundary condition to the solid surfaces, we obtain:

$$\partial\phi/\partial n = -\boldsymbol{U}_\infty \cdot \boldsymbol{n} \tag{6}$$

Once the Kinematic boundary condition is applied to Eqn. (5), we obtain a linear system to be solved:

$$A\boldsymbol{\phi_b} + B\Delta\boldsymbol{\phi_f} = RHS, \tag{7}$$

where $A = \left(a_{ij}\right)_{N\times N}$ is the dipole induced potential coefficient matrix due to the body panels. $\boldsymbol{\phi_b} = \left(\phi_{b,j}\right)^T$ is the vector of dipole strength on the body panels, which is the unknown to be solved for. $B = (b_{ik})_{N\times 2}$ is the dipole induced potential coefficient matrix due to the first wake/LEV panels to the control point of ith body panel, $k = 1$, corresponding to the trailing edge wake, and $k = 2$ corresponding to the LEV. $\Delta\boldsymbol{\phi_f} = [\Delta\phi_1, \Delta\phi_2]^T = [\Delta\phi_W, \Delta\phi_{LEV}]^T$.

$RHS_i = -c_{ij}\,\boldsymbol{U}_\infty \cdot \boldsymbol{n}_{b,j} - w_{ij}\,\Delta\phi_{f,j}$, c_{ij} is the source induced potential coefficient due to the jth body panel to the control point of ith body panel, and $\boldsymbol{n}_{b,j}$ is the normal vector at the jth body panel; w_{ij} is the dipole induced potential coefficient due to the jth wake panel to the control point of ith body panel, and the $\Delta\phi_{f,j}$ is the dipole strength on the jth free wake/LEV panel.

2.2.2 Pressure Kutta condition

At the leading edge and trailing edge, $\Delta\phi_w$ and $\Delta\phi_{LEV}$ are unknowns, which are subjected to pressure Kutta conditions:

$$p_W^+ = p_W^-, \tag{8}$$

$$p_{LEV}^+ = p_{LEV}^-. \tag{9}$$

The p_W^+ and p_{LEV}^+ are the pressures at the positive sides of the wake or LEV; the p_W^- and p_{LEV}^- are the pressure at the negative sides of the wake or LEV. The positive and negative sides of the wake and LEV are defined as shown in Fig.1: the solid surface clockwise before a wake/LEV is in the positive side, the solid surface clockwise after a wake/LEV is in the negative side.

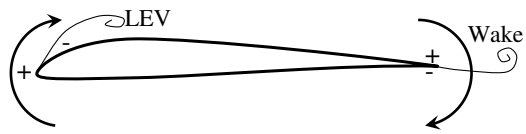

Figure 1: Definition of the positive and negative sides of a trailing edge wake or leading edge vortex.

The physical meaning of Eqn. (8) and (9) is that free vortex sheets cannot bear pressure jump.

For steady status, Eqn. (8) and (9) lead to modified Morino-Kutta condition:

$$\Delta\phi_w = \phi_w^+ - \phi_w^- + \boldsymbol{U}_\infty \cdot \boldsymbol{r}_{TE}, \tag{10}$$

$$\Delta\phi_{LEV} = \phi_{LEV}^+ - \phi_{LEV}^- + \boldsymbol{U}_\infty \cdot \boldsymbol{r}_{LE}, \tag{11}$$

where $\boldsymbol{r}_{TE}$ is the vector from the control point of (-) panel to the (+) panel at the trailing edge, and r_{LEV} is the vector from the control point of (-) panel to the (+) panel at the leading edge.

For unsteady status, Eqn. (8) and (9) have to be enforced through the unsteady Bernoulli Equation:

$$\frac{\partial(\Phi_i^+ - \Phi_i^-)}{\partial t} + \frac{1}{2}(q_i^+)^2 - \frac{1}{2}(q_i^-)^2 = 0, \quad i = 1,2, \tag{12}$$

where $i = 1$ is corresponding to the trailing edge, and $i = 2$ is corresponding to the leading edge, for the convenience of explanation.

From a numerical point of view, the total velocity q_j at the control point of jth body panel is evaluated using a second order finite difference scheme, which is essentially a linear combination of the $\boldsymbol{\phi}_b$:

$$q_i^+ = \boldsymbol{h}_i^{+\boldsymbol{T}}\boldsymbol{\phi_b} + g_i^+, \tag{13}$$

$$q_i^- = \boldsymbol{h}_i^{-\boldsymbol{T}}\boldsymbol{\phi_b} + g_i^-, \tag{14}$$

where $\boldsymbol{h_i^+}$ and $\boldsymbol{h_i^-}$ are column vectors represent the finite difference scheme to evaluated $\partial\phi/\partial s$; g_i^+ and g_i^- are corresponding to the contributions of the inflow velocity. From Eqn. (9), we obtain:

$$q_i^+ = (\boldsymbol{h_i^+}A^{-1})RHS - (\boldsymbol{h_i^+}A^{-1}B)\Delta\boldsymbol{\phi_f} + g_i^+ \tag{15}$$

$$q_i^- = (\boldsymbol{h_i^-}A^{-1})RHS - (\boldsymbol{h_i^-}A^{-1}B)\Delta\boldsymbol{\phi_f} + g_i^+. \tag{16}$$

Also, consider mask vectors $\boldsymbol{m}_i^+$ and $\boldsymbol{m}_i^-$ which extract ϕ_i^+ and ϕ_i^- from the $\boldsymbol{\phi_b}$ vector, where $\boldsymbol{m}_i^+$ is defined a column vector which only has unit element at the same location as ϕ_i^+ in the vector $\boldsymbol{\phi_b}$, other elements are all zero. Similarly, we can also define $\boldsymbol{m}_i^-$:

$$\phi_i^+ = \boldsymbol{m_i^{+T}}\boldsymbol{\phi_b}, \tag{17}$$

$$\phi_i^- = \boldsymbol{m_i^{-T}}\boldsymbol{\phi_b}, \tag{18}$$

From Eqn. (9), we obtain:

$$\phi_i^+ = (\boldsymbol{m_i^+}A^{-1})RHS - (\boldsymbol{m_i^+}A^{-1}B)\Delta\boldsymbol{\phi_f} \tag{19}$$

$$\phi_i^- = (\boldsymbol{m_i^-}A^{-1})RHS - (\boldsymbol{m_i^-}A^{-1}B)\Delta\boldsymbol{\phi_f}. \tag{20}$$

The value of $\boldsymbol{h}_i^{\pm}A^{-1}$ and $\boldsymbol{m}_i^{\pm}A^{-1}$ can be evaluated before the temporal integration for the unsteady problem, and kept constant throughout the simulation.

If the unsteady term in Eqn. (12) is treated with an explicit scheme, the substitution of Eqn. (15)(16) and (19)(20) into Eqn. (12) leads to a quadratic system:

$$\alpha_{ij}\,\Delta\phi_j^2 + \beta_{ij}\,\Delta\phi_j + \gamma_i = 0, \qquad i,j = 1,2, \tag{21}$$

where α_{ij}, β_{ij} and γ_i are coefficients which can be expressed by $\boldsymbol{h}_i^{\pm}A^{-1}$ and $\boldsymbol{m}_i^{\pm}A^{-1}$. Generally, Newton-Raphson method can be used to solve for the system. However, in order to handle the double solutions and none solution scenario, a different approach is proposed in this study.

Eqn. (21) can be rewritten in the following format:

$$\alpha_{ii}\Delta\phi_i^2 + \beta_{ii}\Delta\phi_i + \gamma_i' = 0, \qquad i = 1,2, \tag{22}$$

where $\gamma_i' = \sum_{i\neq j} a_{ij}\Delta\phi_j^2 + \sum_{i\neq j}\beta_{ij}\Delta\phi_j + \gamma_i$. Therefore, Eqn. (22) can be solved as a quadratic equation:

$$\Delta\phi_i = \frac{-\beta_{ii} + \sqrt{\Delta_i}}{2\alpha_{ii}}, \qquad i = 1,2, \tag{23}$$

where $\Delta_i = \max(\beta_{ii}^2 - 4\alpha_{ii}\gamma_i', 0)$ .The solution $(-\beta_{ii} + \sqrt{\Delta_i})/2\alpha_{ii}$ is selected because it recovers the result $\Delta\phi_i = -\gamma_i'/\beta_{ii}$,when $a_{ii} \to 0$.

Through this approach, the quadratic system is solved iteratively. If there is no quadratic term, this approach becomes the Gauss-Seidel method for the linear algebra system. For the 2-D unsteady cases, this scheme converges to 1e-6 within one or two iterations.

2.3 Evaluation of local velocity

Theoretically, the local perturbation velocity $\boldsymbol{u}$ at any point $\boldsymbol{x}_p$ can be evaluated through the following singular integration:

$$\begin{aligned}\boldsymbol{u}_p &= \frac{1}{4\pi}\iint_{S_H}\left[\phi_p\boldsymbol{\nabla}\left(\frac{\partial G(p,q)}{\partial \boldsymbol{n}_q}\right) - \frac{\partial\phi_p}{\partial\boldsymbol{n}_q}\boldsymbol{\nabla}G(p,q)\right]dS \\ &+ \iint_{S_W}\Delta\phi_w(y_q)\boldsymbol{\nabla}\left(\frac{\partial G(p,q)}{\partial\boldsymbol{n}_q}\right)dS \\ &+ \iint_{S_{LEV}}\Delta\phi_{LEV}(y_q)\boldsymbol{\nabla}\left(\frac{\partial G(p,q)}{\partial\boldsymbol{n}_q}\right)dS,\end{aligned} \tag{24}$$

where $\boldsymbol{G}(\boldsymbol{p},\boldsymbol{q})$ is the same Green's function that is defined in Eqn. (5). Practically, the numerical evaluation of Eqn. (24) casts two questions: where and how to evaluate the velocity.

If the field point p is located right on the vortex sheet, Eqn. (24) contains singular integration. For low order panel method, the accurate velocities are expected to appear at the control points of a panel. Lee (2002) implemented this idea in his unsteady wake model for propeller flow. In order to align the wake, the velocities at the nodal points of a panel are interpolated from the velocities from the control points. Re-paneling was carried out at each time step.

However, the velocities are accurate at the control points only if the panels have a regular and smooth geometry. At the late stage of the unsteady LEV evolution, or in certain intermediate steps to determine the steady LEV, the geometry of the vortex sheet could be entangled. The velocity evaluated at the control point of a panel could lead to huge deviation from the exact value. Numerical tests show that evaluating the velocity at nodal point with certain de-singularized vortex kernel turns out to be more robust than the schemes mentioned above.

In 2D, the dipole induced velocity in Eqn. (24) is equivalent to the induced velocity due to a vorticity distribution with strength $\phi/\partial s$:

$$\int \phi\nabla\left(\frac{\partial \ln R}{\partial n}\right)ds = \int \frac{\partial\phi}{\partial s}\frac{\boldsymbol{R}_\perp}{R^2}\,ds\,, \tag{25}$$

where $\boldsymbol{R}_\perp$ is the vector which is perpendicular to $\boldsymbol{R}$, $\boldsymbol{R}_\perp = (-R_y, R_x)$.

Krasny (1987) adopted a de-singularized kernel $\frac{\boldsymbol{R}_\perp}{R^2+\delta^2}$ instead of $\frac{\boldsymbol{R}_\perp}{R^2}$ in Eqn. (25), which led to the *vortex blob method* in the study of the evolution of 2D free vortex sheet. This method, although simple, was successful in many 2D applications. The vortex-induced velocity is limited to a finite value, and the inherent Kelvin-Helmholtz instability is suppressed.

In 3D, the vortex sheet is discretized into constant dipole elements, which are equivalent to vortex loops with constant vorticity strength. Therefore, induced velocity due to the vortex loop can be evaluated using the Biot-Savart law:

$$\begin{aligned}\boldsymbol{u} &= \frac{1}{4\pi}\iint \phi\nabla\left(\frac{\partial\ln R}{\partial\boldsymbol{n}}\right)ds \\ &= \frac{1}{4\pi}\int \phi d\boldsymbol{l}\times\frac{\boldsymbol{R}}{R^3}\ .\end{aligned} \tag{26}$$

Replacing the Biot-Savart kernel $\frac{\boldsymbol{R}}{R^3}$, with the Rosenhead–Moore kernel $\boldsymbol{R}/(R^2+\delta^2)^{3/2}$, leads to the 3D extension of the *vortex blob method.* Studies by Ramsey (1996), He (2010), and Krasny (2001) show that this method can give out reasonable results for the 3D evolution of vortex sheets.

2.4 Alignment schemes

The free vortex sheets shed from the leading edge and trailing edge from a propeller blade are material surfaces, which must be aligned with the local flow velocity. Alignment schemes play very important roles in determining the spatial geometry or distribution of the free vortex sheets.

For the steady and unsteady cases, the alignment schemes are numerically different.

2.4.1 Unsteady alignment

Principally, tracking the evolution of vortex sheets is done in a Lagrangian point of view. Therefore, the unsteady alignment of the free vortex sheet is straightforward.

$$\dot{\boldsymbol{x}}_i = \boldsymbol{f}(\boldsymbol{x}_1, \boldsymbol{x}_2, \dots, \boldsymbol{x}_N) \tag{27}$$

Once we know the velocities at the nodal points of the LEV/wake, we can integrate them to get the trajectory of these points with time. For propeller wake flow, at each time step, new shed wake panels are added into the system, and some wake panels far down steam are trimmed out.

Many studies suggested using Runge-Kutta 4th order scheme for the time marching (e.g., Krasny 1987, Ramsey 1996). The rolling-up details of the vortex sheets cannot be captured by the Euler-Explicit scheme, which always keeps increasing the rotating radius of the discrete points

on the vortex sheet around the center of rolling-up. However, for 3D applications, RK-4 scheme could be too expensive. Studies by Lee (2002, 2004) and He (2010) showed that if the details of the rolled up wake are of little importance, in a $\boldsymbol{U}_\infty$ convection dominant flow field, such as propeller wake flow, careful application of Euler-Explicit scheme can lead to satisfactory results.

2.4.2 Steady alignment

The steady propeller performances are more interesting to the engineering community. As an analogy to the Euler-Explicit scheme for the unsteady cases, many researchers align the vortex sheet using the velocity at the upstream nodal points:

$$\begin{aligned} x_{i+1} &= x_i + \Delta x \\ y_{i+1} &= y_i + \frac{q_{y,i}}{q_{x,i}}\Delta x \\ z_{i+1} &= z_i + \frac{q_{z,i}}{q_{x,i}}\Delta x \end{aligned} \tag{28}$$

Numerical tests show that this scheme is stable, and converges fast. However, this scheme has the same deficiency as the Euler-Explicit scheme for the unsteady alignment; that is, that it will continuously enlarge the rotating radius around the center of rolling-up. For the simulation of LEV, the spatial distribution of the vortex sheet is more important than that for the trailing edge wake. The study in this paper reveals that the location and size of the rolling-up region is closely related to the pressure distribution on the solid surface. Unfortunately, the scheme described in Eqn. (28) cannot predict the correct location and size of the rolling-up region. Therefore, in order to get better prediction of the pressure distribution on the solid surface, alignment scheme in a manner of trapezoidal rule is preferred. However, direct application of the trapezoidal rule turned out to be unstable.

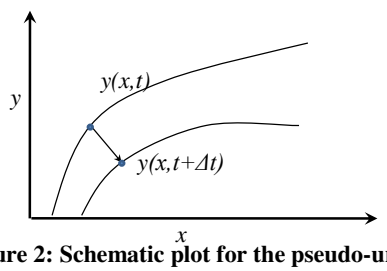

Figure 2: Schematic plot for the pseudo-unsteady approach of alignment.

In this study, a pseudo-unsteady approach applying the trapezoidal rule is proposed. As shown in Fig. 2, consider a material line defined as:

$$\begin{aligned} y &= y(x,t) \\ z &= z(x,t). \end{aligned} \tag{29}$$

We have:

$$\begin{aligned} q_y &= \frac{Dy}{Dt} = \frac{\partial y}{\partial t} + q_x\frac{\partial y}{\partial x} \\ q_z &= \frac{Dz}{Dt} = \frac{\partial z}{\partial t} + q_x\frac{\partial z}{\partial x} \end{aligned} \tag{30}$$

which leads to:

$$\begin{aligned} \frac{\partial y}{\partial t} &= q_y - q_x\frac{\partial y}{\partial x} \\ \frac{\partial z}{\partial t} &= q_z - q_x\frac{\partial z}{\partial x} \end{aligned} \tag{31}$$

Discretizing Eqn. (31) with the finite difference scheme for the slopes, and with the Euler-Explicit scheme for the unsteady terms, we have:

$$\begin{aligned} y_i^{n+1} &= y_i^n + \frac{\Delta t}{2}\Big[\left(q_{y,i-1}^n + q_{y,i}^n\right) \\ &\qquad - \left(q_{x,i-1}^n + q_{x,i}^n\right)\frac{y_i^n - y_{i-1}^n}{x_i^n - x_{i-1}^n}\Big] \\ z_i^{n+1} &= z_i^n + \frac{\Delta t}{2}\Big[\left(q_{z,i-1}^n + q_{z,i}^n\right) \\ &\qquad - \left(q_{x,i-1}^n + q_{x,i}^n\right)\frac{z_i^n - z_{i-1}^n}{x_i^n - x_{i-1}^n}\Big]. \end{aligned} \tag{32}$$

Eqn. (32) is applied along all the vortex lines shed from the leading edge and trailing edge of a propeller blade.

The merits of Eqn. (32) are obvious: 1) for the convection dominant flow, $q_{x,i-1}^n + q_{x,i}^n$ are usually positive, and therefore, the gradients are evaluated in an upwind manner, which is stable; 2) if a steady status is reached, the vortex lines are aligned in a trapezoidal manner, which keeps the correct radius for helical geometry. There are also drawbacks for this scheme: 1) it converges slowly; and 2) the strictly defined steady status may not be reached.

2.4 Interaction with solid surface

The most significant difference between the LEV and trailing edge wake is that the evolution of LEV strongly interacts with the solid surface, whereas the trailing edge wake is located in a large and unbound domain.

For potential based panel methods, once the wake/LEV panels penetrate the solid surface, the simulation blows up. A numerical fence is applied in order to keep the simulation going on (He 2010).

3 APPLICATION TO 2D BI-CONVEX FOIL

The LEV model is first applied to a 2D bi-convex foil, which has a parabolic thickness distribution, $t_{\max}/c = 10\%$. The sharp leading edge of this foil creates leading edge vortex sheet, which will be convected downstream, and interact with the suction side surface of the foil. In this case, only the unsteady behavior can be investigated.

Here we are mainly interested in the early stage evolution of the LEV after its inception.

The pressure kutta condition and de-singularized scheme with δ are applied. Runge-Kutta 4th order scheme is used to trace the LEV and also the trailing edge wake.

On the foil surface, 1000 panels with cosine spacing are distributed. The inflow angle of attack is 5 degrees. In order to investigate the effects of the de-singularized parameter δ, two values, $\delta/c = 0.0005, 0.0003$ are tested. The time step size Δt is set to be $0.000125c/U_\infty$.

The results by the inviscid finite volume method were also obtained from the commercial software Fluent. The Fluent simulation took around 1 hour for 1000 time steps with 24 Intel Xeon 2.54GHz CPUs. The BEM model took 20 ~ 40 minutes on a Single Intel Xeon 2.54GHz CPU.

Fig. 4 shows the comparison of the LEV geometry at a very early stage from current model with the results from the inviscid FVM. A re-paneling scheme is adopted in this simulation – if the length of a panel is longer than a threshold, a new point will be inserted into the panel using a local cubic Lagrangian interpolation. Clearly, the result from the smaller δ agrees better with the FVM result, but is less smooth than result from the larger δ.

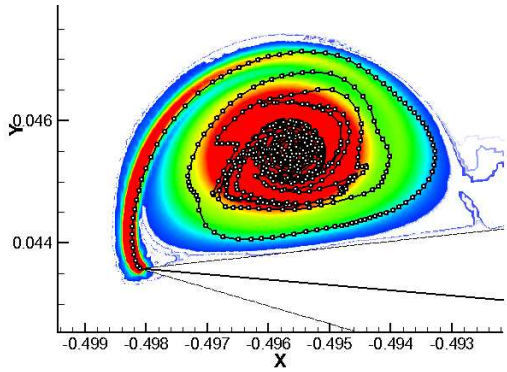

(a)

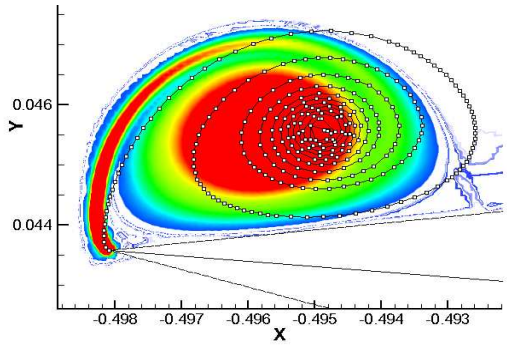

(b)

Figure 4: Comparisons of the LEV geometry, t=0.0125c/U (symbols are results from current schemes; color maps are contours of vorticity magnitude from inviscid FVM; a: $\delta = 0.0003c$; b: $\delta = 0.0005c$)

Fig. 5 and 6 show the corresponding comparisons of the pressure distribution. In most part of the foil, the pressure are not affected by the LEV, the results from panel methods and the inviscid FVM agree extremely well, whereas the LEV does affect the pressure very close to the leading edge. A low pressure spike is formed in a very narrow region. The zoom-in views are consistent with Fig. 4 – better correlation of the location and size of the LEV predicts better correlation of the pressure distribution. It is also worthwhile to point out that both the panel method and FVM predict pressure coefficient greater than 1, which is related to the unsteadiness.

The results at a later stage are also investigated. Only the larger δ are adopted for the later stage evolution. The LEV geometry from the smaller δ configuration is too complex to handle. As shown in Fig. 7 and 8, although the detailed structure of the LEV from current scheme are convoluted, the spatial distribution of the LEV from both methods compare well. The pressure distributions are also reasonably close, as expected. The difference of the magnitude of the –Cp may related to the numerical dissipation of the inviscid FVM.

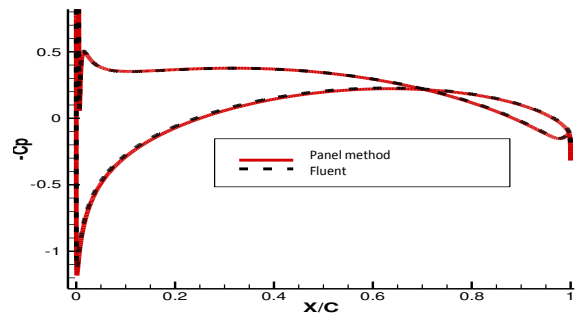

(a)

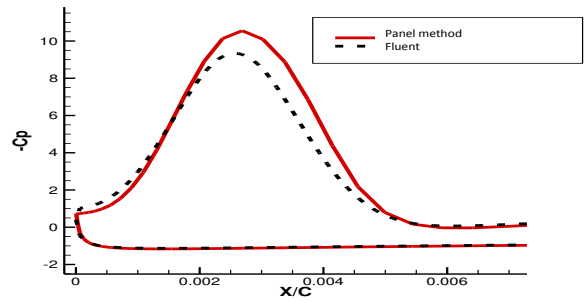

(b)

Figure 5: comparisons of the pressure distribution, t=0.0125c/U, $\delta = 0.0003c$ (a: the overall distribution; b: a zoom-in view close to the leading edge.)

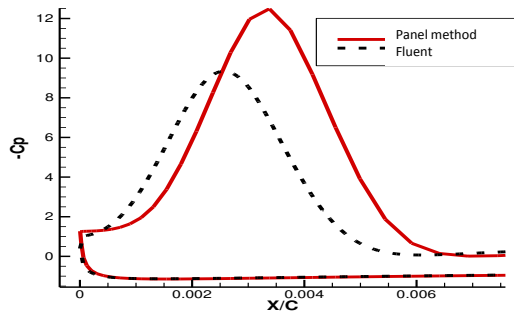

Figure 6: Comparisons of the pressure distribution, t=0.0125c/U, $\delta = 0.0005c$ (a zoom-in view close to the leading edge).

Comparisons with RANS are also carried out. The RANS are carried out using the same grid as in the inviscid FVM cases. $k - \omega$ turbulent model is adopted, and the wall y+ are mainly controlled under 5. In contrast with the inviscid FVM, at the very early stage, the LEV geometry from $\delta = 0.0005c$ compares better with the RANS results than that from $\delta = 0.0005c$. However, although the location of the low pressure peak seems to be predicted correctly, current schemes apparently overestimated the magnitude of –Cp, as shown in Fig. 9 and 10.

The investigations in 2D reveal some effects of the de-singularized parameter δ . To a certain extent, it represented the diffusive effect of the viscosity, which spreads the vortex sheet into a larger region. However, another important effect of the viscosity – dissipation does not incorporate into the current scheme. This explains why the current scheme always over-predicts the magnitude of the low pressure peak comparing with the RANS results.

It is worthwhile to point out that in 2D, the LEV model is principally through a Lagrangian point of view. Therefore, the steady state cannot be well defined. Due to the lack of dissipation, energy carried by vortex points keep entering and accumulating in the rolling-up region. The unbound energy finally makes the model blow up.

Also, the current spatial and temporal discretization are very fine, in order to resolve the inception process of the LEV, which is extremely local. Finer resolution was also tested, and was found to give similar LEV geometry as long as δ is kept the same.

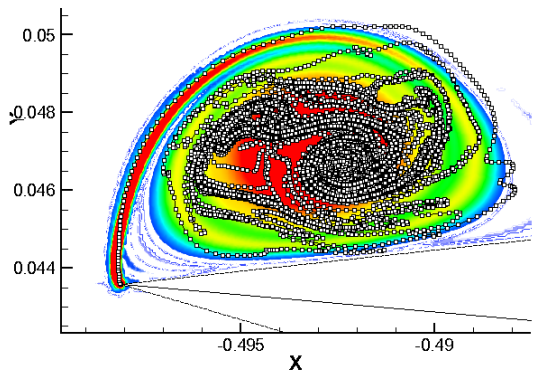

Figure 7: Comparisons of the LEV geometry, t=0.04c/U, $\delta = 0.0005c$ (symbols are results from current schemes; color maps are contours of vorticity magnitude from inviscid FVM).

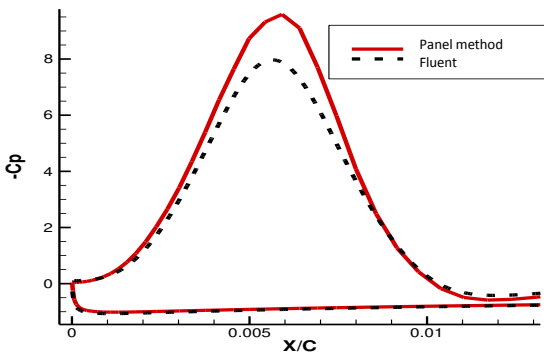

Figure 8: Comparisons of the pressure distribution, t=0.04c/U, $\delta = 0.0005c$ (a zoom-in view close to the leading edge).

4 APPLICATION TO A 3D WINGS

In 3D, an advantage over 2D is that the rolling-up of the LEV is in the y-z plane, and the convection mainly happens in the chord-wise direction. Therefore, a steady status can be well defined. However, in 3D we cannot achieve the same fine resolution as that we used in the 2D study. Correspondingly, the de-singularized parameter δ cannot be too small; otherwise the results cannot be stabilized. According to Krasny (1987), δ has to be greater or at least at the same order of the grid size. On the other hand, 2D studies (Krasny 1987) indicate that the different size of δ could result in a similar geometry of the vortex filaments for a long time evolution.

In the following study, δ is chosen according to the grid size, but further investigation of the effects of different δ is needed in the future.

The 3D steady LEV model is then applied to 3D wings. The chord-wise direction corresponds to the x direction, and the span-wise direction corresponds to the y direction.

4.1 LEV shed from a delta wing

Delta wings are well-known for strong LEV effects. In order to test the model, a delta wing with parabolic thickness distribution is investigated. Same as in the 2D biconvex foil case, at each section, maximum thickness is set to be 10% of the chord length. The aspect ratio of this delta wing is 1. The inflow AOA is 15 degrees.

Both the Euler-Explicit like scheme and the pseudo-unsteady scheme are applied. RANS simulation with $k-\omega$ SST turbulent model is also carried out with commercial software Fluent. The RANS case using 5 million cells took 10 hours to converge, with 32 Intel Xeon 2.54GHz CPUs. The wall y+s are mainly controlled in the range between 30 and 80. The BEM model took around 2 hour on a single CPU of the same type to reach the steady status.

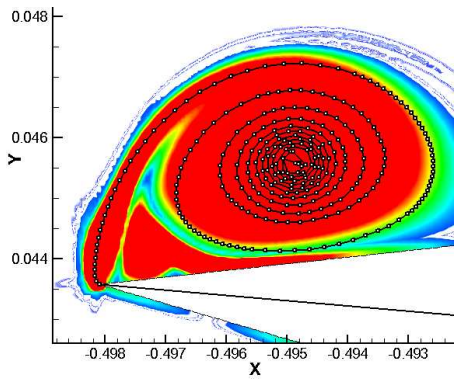

Figure 9: Comparisons of the LEV geometry, t=0.0125c/U, $\delta = 0.0005c$ (symbols are results from current schemes; color maps are contours of vorticity magnitude from RANS).

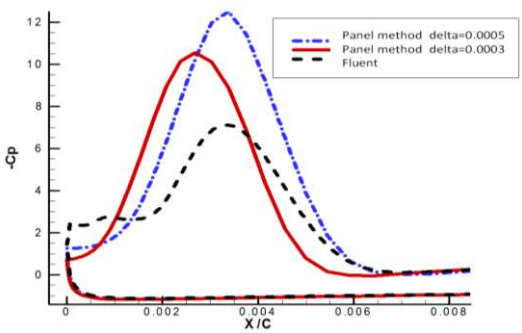

Figure 10: Comparisons of the pressure distribution with RANS, t=0.0125c/U (a zoom-in view close to the leading edge).

Fig. 11 shows the LEV geometries predicted from both Euler-Explicit like scheme and pseudo-unsteady scheme. The corresponding streamlines from RANS is also plotted in Fig. 11(c). Obviously, the pseudo-unsteady scheme correlated better with the RANS result than with the Euler-Explicit like scheme.

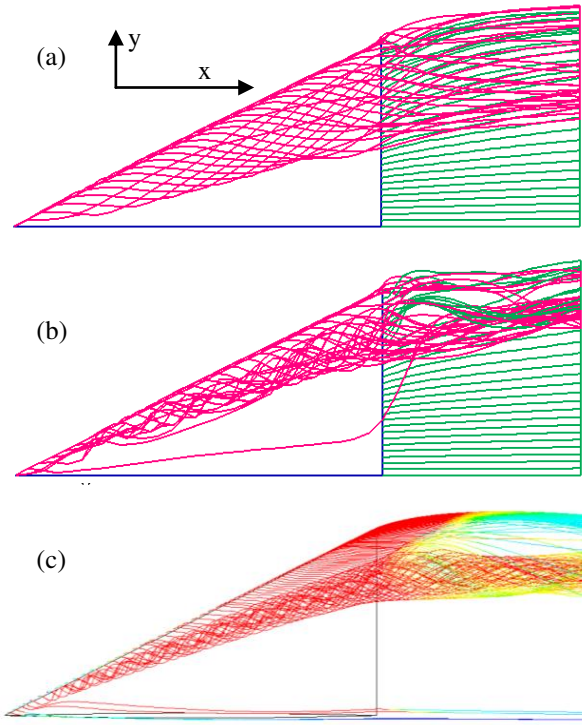

Figure 11: LEV geometry (a:Euler-Explicit like scheme; b: pseudo-unsteady scheme; c: RANS streamlines released from leading edge.)

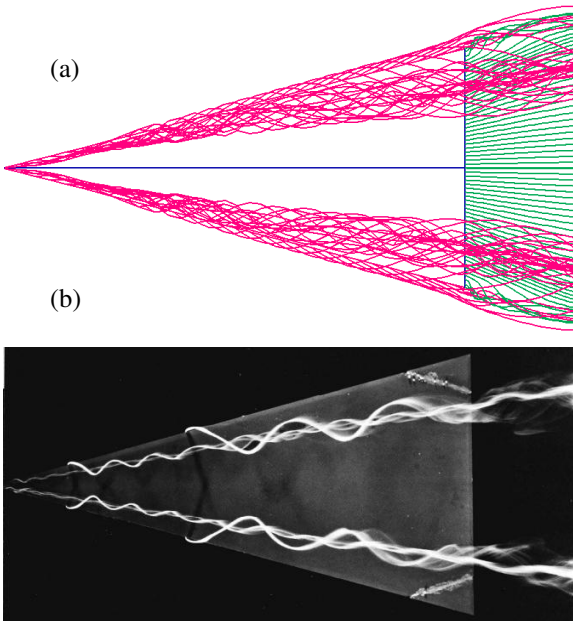

Figure 12: LEV geometry (a: pseudo-unsteady scheme for a thin wing of 15DEG semi-vertex angle at 20DEG AOA; b: corresponding experimental picture for d, after Van Dyke 1982, Fig. 90).

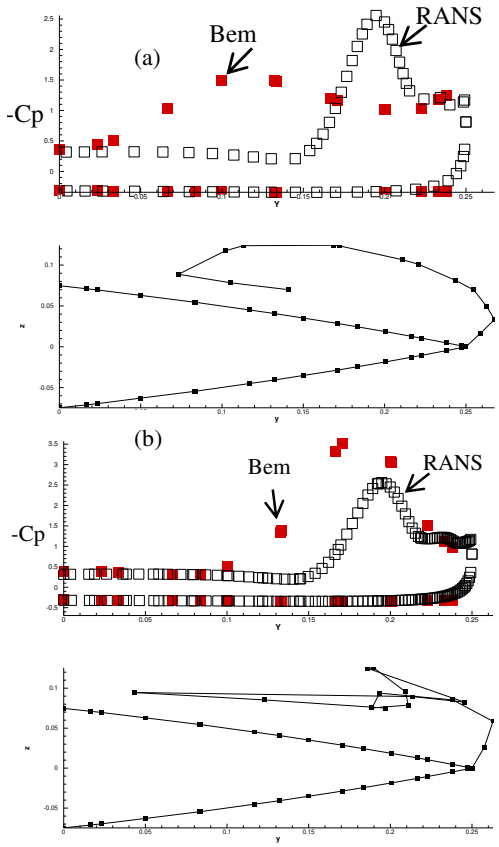

Figure 13: Comparisons with RANS, x/c=-1.5 (a:Euler-Expilict like scheme; b: pseudo-unsteady scheme.)

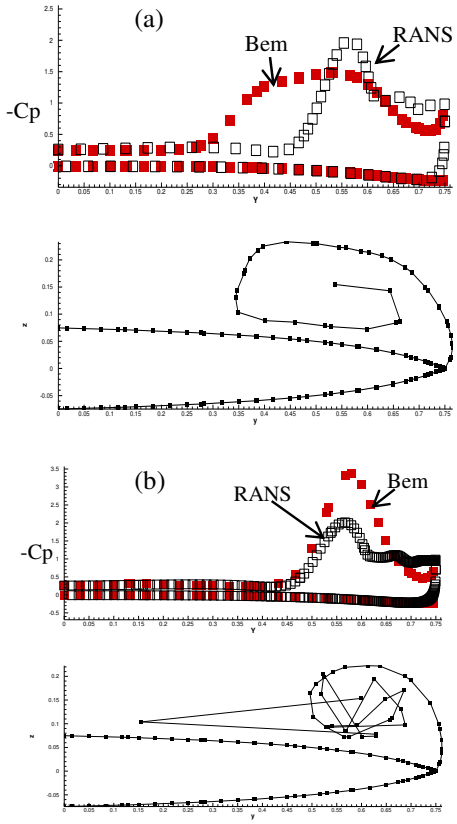

Figure 14: Comparisons with RANS, x/c=-0.5 (a: Euler-Expilict like scheme; b: pseudo-unsteady scheme).

Fig. 12 compares the LEV geometries predicted from the pseudo-unsteady scheme with the experimental observation. In this case, the flow around a thin delta wing with a 15DEG semi-vertex angle at 20DEG AOA is simulated. The results agree well with the experimental observation, as shown in Fig 12(b), after Van Dyke's *An Album of Fluid Motion,* Fig. 90.

Two span-wise cross-sections are taken to make detailed comparisons for the cases shown in Fig. 11(x/c=-1.5, -0.5). As shown in Fig. 13 and 14, although the Euler-Explicit like scheme predicts a smoother LEV geometry than the pseudo-unsteady scheme, the latter has better correlation with the pressure distribution from RANS. The location of the low pressure peak seems to be captured by the latter; however, the magnitude is still overshot.

4.2 Tip-swept wing

A tip-swept wing, which is expected to better resemble a propeller blade is also investigated. As shown in Fig. 15, sweep is superimposed onto a elliptic planform, which has an aspect ratio $AR = 1.57$. All the sections of the wing have NACA0010 thickness form, without camber.

Before applying the LEV model, the results at low AOA from current BEM model is validated with RANS, which is obtained through commercial software Starccm+.

$k - \omega$ SST turbulent model is adopted, and the wall y+ are mainly controlled in the range between 30 and 80. For the convenience of grid generation, the trailing edge of the wing is made to be round. The RANS case took around 3 hours with 16 Intel Xeon 2.54GHz CPUs to converge. The BEM code took 3 minutes on a single CPU of the same type to get the results.

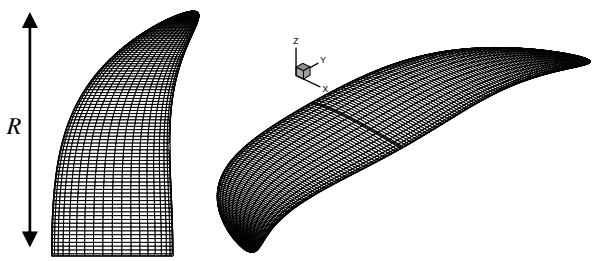

Figure 15: Geometry of the tip-swept wing.

Fig. 16 shows the comparison of the pressure distributions predicted by current BEM model without LEV model and the RANS results, at AOA=2DEG. A very good agreement can be observed, even very close to the tip of the wing. Because the wing has round trailing edge, the pressure therefore has a kink as expected.

For large AOA, the LEV model is attempted to be applied. Visually reasonable LEV and wake geometry is obtained, as shown in Fig. 17. However, detailed comparisons with RANS are not carried out.

5 LEV EFFECTS ON A PROPELLER.

A preliminary application of current set of schemes is attempted to a five-bladed, no-skew no-rake propeller. (Propeller 4381, Boswell 1971)

For the propeller application, the starting point of the LEV is not known, and is expected to be determined by either empirical formulation (Greeley 1982) or coupling with boundary layer solver. In this study, the starting point of the LEV is assumed to be at $0.98R$. It took 2 hours on a single CPU to get the results.

.

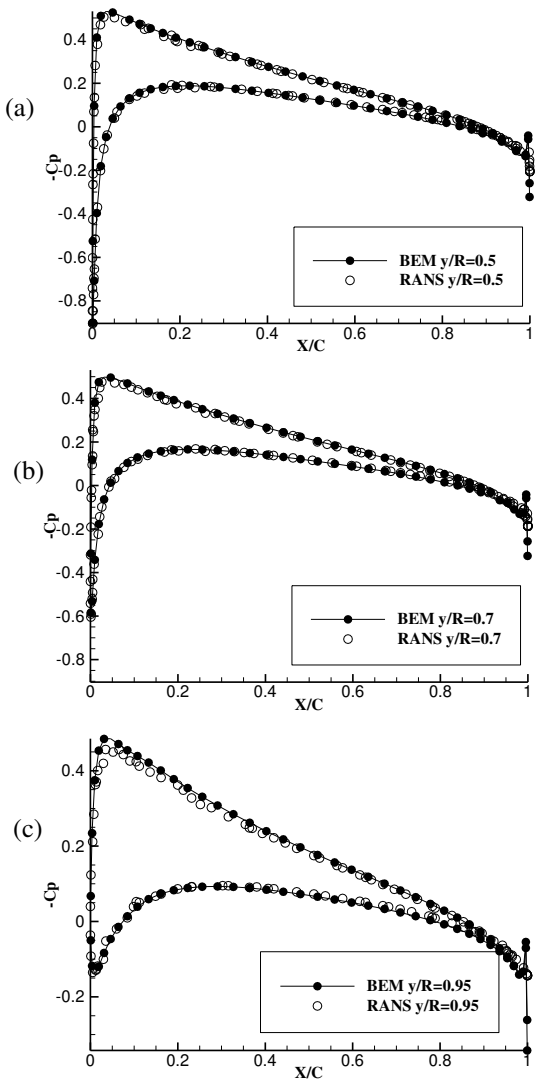

Figure 16: Comparisons of pressure distributions at different strip, AOA=2DEG. No LEV in this case.

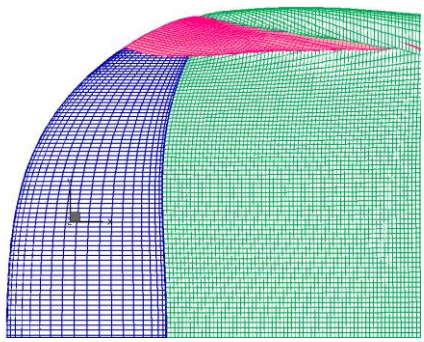

Figure 17: LEV and wake geometry of the tip-swept wing, AOA=15DEG.

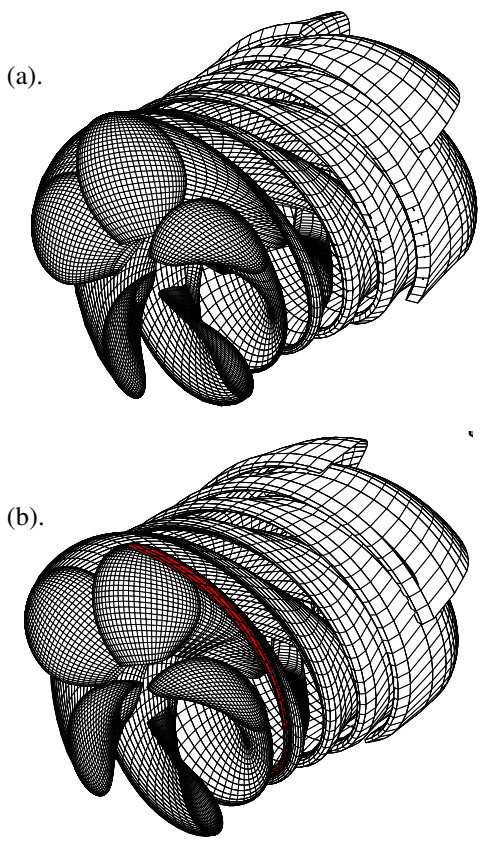

Figure 18: Wake geometries with and W/O LEV at $J_s = 0.6$ (a:without LEV; b: with LEV, only the LEV at the key blade is shown)

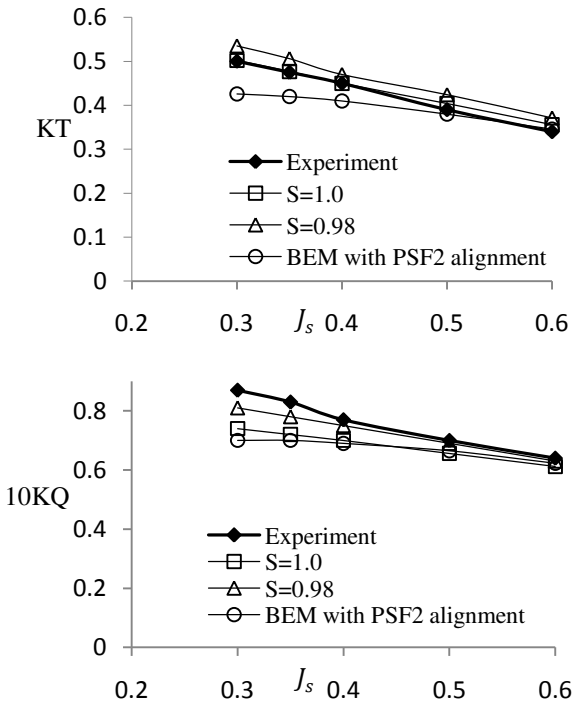

Figure 19 : KT and 10KQ for 4381 propeller. *S* is the location at which y/R the LEV starts. Experimental data are extracted from (Boswell, 1971). PSF-2 alignment is according to Greeley and Kerwin (1982).

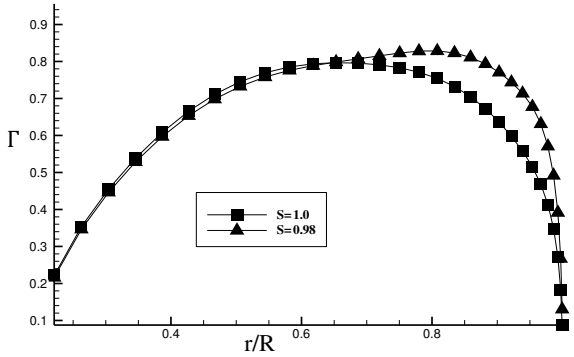

Figure 20. Circulation distributions with the LEV model.

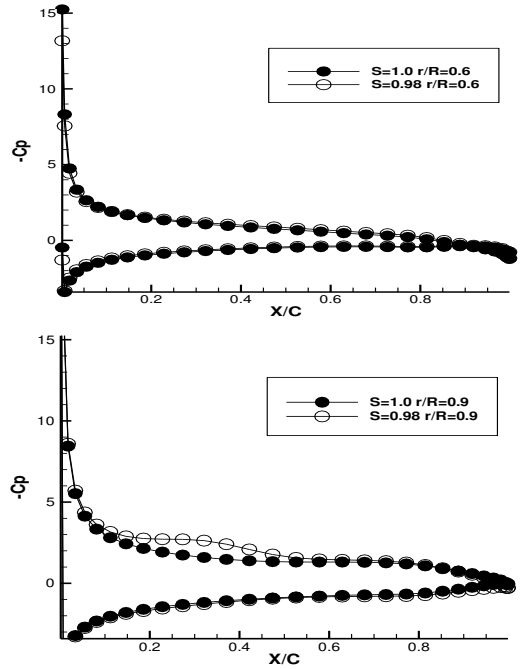

Figure 21. LEV effects on the pressure distributions, where $Cp = (p - p_0)/(\frac{\rho}{2} n^2 D^2)$

Fig. 18 shows the geometry of the wake without/with LEV at $J_s = 0.6$. Only the LEV shed from the key blade is plotted. Fig. 19 shows the integrated force of the propeller at different J_s, with or without LEV model, where PSF2 referring to the fast wake alignment scheme by Greeley and Kerwin (1982), and S=1 corresponding to full wake alignment without LEV. Since the BEM model without LEV gives good predictions of KT and KQ when J_s is greater 0.6, physically no LEV is expected. Only J_s less than 0.6 is considered in the simulation.

The trend of change of the integrated force is consistent with our intuition. LEV leads to larger forces. For the value of KT, it seems that the aligned wake without LEV does a good job, especially for the low J_s cases, at which the influence of the wake shed from other blades could be significant.

The LEV model over-predicted the KT. However, for the value of KQ, without LEV models, we underestimate the value comparing with the experimental data. With the LEV model, the prediction of KQ is improved. Also we

can find that the higher the loading, the more significant influence it has on the propeller performance.

The circulations of the propeller at $J_s = 0.4$ are shown in Fig.20. Clearly the LEV redistributed the loading on the blade. The loading close to the tip is amplified, and the loading towards to the hub is weakened.

Fig. 21 shows the pressure distributions with and without LEV model at two different strips. As we can see, close to the tip, the LEV creates a low pressure plateau on the back side of the blade, which contributes to the increment of predicted forces

A few remarks should be made on the current application of the LEV model to propeller geometries. Although qualitatively the results seem reasonable, quantitatively more investigation is required to verify the model. The predicted KT and KQ do not approach to the experimental data at the same time. This might be related to the Kutta condition at the leading edge, and also the discretization error. For the sharp leading edge in the delta wing case, the Kutta condition is expected to be accurate. But for a round leading edge, due to the boundary layer behavior the Kutta condition is ambiguous. Katz's (2001) study on the stall flow of 2D airfoils suggested that a reduction coefficient was required for Kutta condition of the separation. However, this coefficient is determined by experience.

Also, the study in this paper does not consider the viscous effects carefully, which is expected to be handled in a more rigorous way, such as coupling with a boundary layer solver.

6 CONCLUSIONS AND FUTURE WORK

In this a paper, a numerical model is developed to simulated the LEV effects on the propeller performance. The model is first applied to 2D and 3D wings, and then a propeller. Preliminary results show that this model is able to predict the LEV to a certain extent. However, more systematic study is demanded to validate this model and help make it to become a practically useful tool.

In 2D, hydrofoils with round leading edge will be studied in order to understand the Kutta condition of the LE detachment point better.

In 3D, convergence study will be carried out, in order to show the grid-independence of the set of schemes proposed in this paper. Viscous/Inviscid interactive method should be developed to determine the starting point of separation.

In terms of RANS, different turbulent models will be tested. For the application to the propeller flow, correlations with RANS are planned as well.

ACKNOWLEDGEMENT

Support for this research was provided by the U.S. Office of Naval Research (Contract No. N00014-07-1-0616 and N0014-10-1-0931) and Phases V and VI of the "*Consortium on Cavitation Performance of High Speed Propulsors*" with the following current members: American Bureau of Shipping, Daewoo Shipbuilding and Marine Engineering Co. Ltd., Kawasaki Heavy Industry Ltd., Rolls-Royce Marine AB, Rolls-Royce Marine AS, Samsung Heavy Industries Co. Ltd., SSPA AB, Sweden, VA Tech Escher Wyss GmbH, Wärtsilä Propulsion Netherlands B.V., Wärtsilä Propulsion Norway AS, Wärtsilä Lips Defense S.A.S., and Wärtsilä CME Zhenjiang Propeller Co. Ltd.

REFERENCES

Boswell, R.J. (1971). Design, Cavitation Performance, and Open-Water Performance of a Series of Research – Skewed Propellers. Naval ship research and development center. Department of the Navy.

Greeley, D.S. (1982). Marine propeller blade tip flows. PH.D dissertation, MIT.

Van Dyke, M. (1982). An Album of Fluid Motion. The Parabolic Press, pp. 54.

Greeley, D. S. & Kerwin, J. E. (1982). Numerical methods for propeller design and analysis in steady flow. Transactions of Society of Naval Architects & Marine Engineers, **90**, pp. 415-453.

Krasny, R. (1987). Computation of vortex sheet roll-up in the Trefftz plane. Journal of Fluid Mechanics. **184**, pp.123-155.

Ramsey, W. D. (1996). Boundary Integral Methods for Lifting Bodies with Vortex Wakes. PH.D dissertation, MIT.

Lindsay, K. & Krasny, R. (2001). A Particle Method and Adaptive Treecode for Vortex Sheet Motion in Three-Dimensional Flow. Journal of Computational Physics **172**, pp.879-907.

Katz, J. & Plotkin, A. (2001). Low-Speed Aerodynamics(second edition). Cambridge University Press, pp. 510-516.

Lee, H.S. (2002). Modeling of unsteady wake alignment and developed tip vortex cavitation. PH.D dissertation, UT Austin.

Lee , H.S. & Kinnas, S. A. (2004). 'Application of boundary element method in the prediction of unsteady blade sheet and developed tip vortex cavitation on marine propellers'. Journal of Ship Research **48**(1), pp.15-30.

Singh, S. (2009). Viscous/Inviscid flow around 2-D and 3-D hydrofoils with emphasis on leading edge flow separation. Master thesis, UT Austin.

He, L. (2010). Numerical Simulation of Unsteady Rotor/Stator Interaction and Application to Propeller/Rudder Combination. PH.D dissertation, UT Austin.